

## Lab-on-a-contact lens platforms fabricated by multi-axis femtosecond laser ablation

Moreddu, Rosalia; Nasrollahi, Vahid; Kassanos, Panagiotis; Dimov, Stefan; Vigolo, Daniele; Yetisen, Ali

DOI:  
[10.1002/smll.202102008](https://doi.org/10.1002/smll.202102008)

License:  
Other (please specify with Rights Statement)

*Document Version*  
Peer reviewed version

*Citation for published version (Harvard):*  
Moreddu, R, Nasrollahi, V, Kassanos, P, Dimov, S, Vigolo, D & Yetisen, A 2021, 'Lab-on-a-contact lens platforms fabricated by multi-axis femtosecond laser ablation', *Small*, vol. 17, no. 38, 2102008.  
<https://doi.org/10.1002/smll.202102008>

[Link to publication on Research at Birmingham portal](#)

### **Publisher Rights Statement:**

This is the peer reviewed version of the following article: [See <https://doi.org/10.1002/smll.202102008> for full citation], which has been published in final form at [Link to final article using the DOI]. This article may be used for non-commercial purposes in accordance with Wiley Terms and Conditions for Use of Self-Archived Versions. This article may not be enhanced, enriched or otherwise transformed into a derivative work, without express permission from Wiley or by statutory rights under applicable legislation. Copyright notices must not be removed, obscured or modified. The article must be linked to Wiley's version of record on Wiley Online Library and any embedding, framing or otherwise making available the article or pages thereof by third parties from platforms, services and websites other than Wiley Online Library must be prohibited.

### **General rights**

Unless a licence is specified above, all rights (including copyright and moral rights) in this document are retained by the authors and/or the copyright holders. The express permission of the copyright holder must be obtained for any use of this material other than for purposes permitted by law.

- Users may freely distribute the URL that is used to identify this publication.
- Users may download and/or print one copy of the publication from the University of Birmingham research portal for the purpose of private study or non-commercial research.
- User may use extracts from the document in line with the concept of 'fair dealing' under the Copyright, Designs and Patents Act 1988 (?)
- Users may not further distribute the material nor use it for the purposes of commercial gain.

Where a licence is displayed above, please note the terms and conditions of the licence govern your use of this document.

When citing, please reference the published version.

### **Take down policy**

While the University of Birmingham exercises care and attention in making items available there are rare occasions when an item has been uploaded in error or has been deemed to be commercially or otherwise sensitive.

If you believe that this is the case for this document, please contact [UBIRA@lists.bham.ac.uk](mailto:UBIRA@lists.bham.ac.uk) providing details and we will remove access to the work immediately and investigate.

# Lab-on-a-Contact Lens Platforms Fabricated by Multi-Axis Femtosecond Laser Ablation

*Rosalia Moreddu,<sup>a,b,\*</sup> Vahid Nasrollahi,<sup>c</sup> Panagiotis Kassanos,<sup>d</sup> Stefan Dimov,<sup>c</sup> Daniele  
Vigolo,<sup>b,ef</sup> Ali K. Yetisen<sup>a</sup>*

<sup>a</sup> Department of Chemical Engineering, Imperial College London, London SW7 2AZ, UK

<sup>b</sup> School of Chemical Engineering, University of Birmingham, Birmingham B15 2TT, UK

<sup>c</sup> Department of Mechanical Engineering, University of Birmingham, Birmingham B15 2TT, UK

<sup>d</sup> Hamlyn Centre, Institute of Global Health Innovation, Imperial College London, London SW7  
2AZ, UK

<sup>e</sup> School of Biomedical Engineering, University of Sydney, Sydney, NSW 2006, Australia

<sup>f</sup> The University of Sydney Nano Institute, University of Sydney, Sydney, NSW 2006, Australia

**Keywords:** Contact Lenses, Femtosecond Laser Ablation, Microfluidics, Wearable Sensors,

Lab-on-a-Chip

## **Abstract**

Contact lens sensing platforms have drawn interests in the last decade for the possibility of providing a sterile, fully integrated ocular screening method. However, designing scalable and convenient processing methods while keeping a high resolution is still an unsolved challenge. In this article, femtosecond laser writing was employed as a rapid and precise method to engrave microfluidic networks into commercial contact lenses. Functional microfluidic components such as flow valves, resistors, multi-inlet geometries, and splitters were produced using a bespoke 7-axis femtosecond laser system, yielding a resolution of 80  $\mu\text{m}$ . The ablation process and the tear flow within microfluidic structures was evaluated both experimentally and computationally using finite element modeling. Flow velocity drops of the 8.3%, 20.8%, and 29% were observed in valves with enlargements of the 100%, 200% and 300%, respectively. Resistors yielded flow rate drops of 20.8% 33% and 50% in the small, medium, and large configurations, respectively. Two applications were introduced, namely a tear volume sensor and a tear uric acid sensor (sensitivity 16  $\text{mgL}^{-1}$ ), which are both painless alternatives to current methods and provide reduced contamination risks of tear samples.

## Introduction

The World Health Organization reports that in 2020 approximately 2.2 billion people worldwide suffered of ocular impairment caused by a number of preventable factors, including age-related macular degeneration, cataracts, infectious diseases of the cornea, trachoma, and systemic diseases like diabetes.<sup>1</sup> Despite ophthalmology being one of the busiest departments in public and private hospitals worldwide, the lack of technological innovation in the field results in the inability to address these problems timely and effectively.

Currently, ocular health screening is carried out one-off only by physicians in clinics, using expensive machinery which set a global screening standard based on reaction over prevention. Extensive investigations on the tear fluid composition revealed the potential of this body fluid in the prevention and monitoring of both ocular and systemic diseases, accompanied by the possibility to be collected painlessly and non-invasively.<sup>2,3</sup>

At present, the gold standards for tear fluid collection are the Schirmer's test and the capillary tube methods.<sup>3</sup> The Schirmer's test consists on inserting a paper strip in the lower eyelid of the patient's eye for five minutes. A large number of studies agree on the low reliability of such test as a tear sampling method, due to the compositional variations in the tear fluid induced by local irritation of the eye, as well as by contaminants introduced by further extraction of the fluid from the paper strip.<sup>4,6</sup> In addition, tear fluid extraction and laboratory analysis are expensive and time-consuming procedures. The Schirmer's test is also largely used to aid the diagnosis of dry eye disease, by evaluating the amount of tear fluid collected.<sup>3,4,6</sup> This methodology has also been considered obsolete and often unreliable, given that the presence of an external body in the lower eyelid induces tear overflow, leading to false positive results.<sup>4,6</sup> The capillary tube method involves a similar process where the tear fluid is collected in a glass or plastic tube, and further stored in a

sterile container. This partially overcomes the problems of contamination, but keeps the disadvantages associated to external tear analysis.

The need for innovation in ophthalmology drives the development of alternative solutions to painlessly and precisely sample and analyse the tear fluid. Contact lenses can be a suitable platform to embed such functionalities, being already used by 150 million people worldwide for vision correction and cosmetics.<sup>3</sup>

Microfluidic contact lenses have thus attracted particular interest in the last few years, due to their potential of allowing on-eye, real-time tear fluid processing.<sup>7-10</sup> The crucial advantages lie on the reduced contamination risks compared to current methods, fast analysis times at point-of-care settings, and the possibility of achieving continuous monitoring.<sup>9, 11, 12</sup>

Recent studies report the development of enhanced contact lens devices.<sup>7-10, 12-17</sup> However, most of them rely on processes that are not scalable. Lab-made microfluidic contact lenses in the literature are primarily based on replica moulding of hydrogels into curved surfaces.<sup>10</sup> It is intuitive that such processes present several limitations: they use materials which are different from the complex polymers patented by contact lens companies and utilised in contemporary contact lens manufacturing, they require days of work to produce a single device, and for this reason they also lack repeatability. Laser ablation has been previously used to produce structures in contact lenses by direct writing. For example, a CO<sub>2</sub> laser was used to inscribe microfluidic structures into soft contact lenses.<sup>18</sup> However, soft contact lenses are obtained by hydrophilic materials made of poly-HEMA as the core polymer, which makes them unsuitable to be used as microfluidic platforms (e.g. the liquid spreads all over the contact lens instead of following a predictable flow pattern within the microfluidic network). In this context, rigid contact lenses represent a more suitable option.<sup>3, 7</sup> They are made of hydrophobic silicone acrylates, making them easier to handle and process.<sup>3</sup> We

previously demonstrated the possibility of incorporating sensors within microcavities or millifluidic channels in contact lenses for ocular temperature and tear analytes monitoring.<sup>7, 8, 12</sup> These processes involved the use of paper-assisted fluid flow, and inscription was performed by CO<sub>2</sub> laser ablation, yielding larger and irregular structures, that do not allow to integrate complex networks in a single device.

Femtosecond laser ablation allows to directly write small features (down to 30 μm of width) in a single step (**Figure 1A**). The inscription takes place by cold ablation, i.e. athermal laser-material interaction regime, rather than a thermal one with a heat affected zone and various negative side effects. In particular, the laser emits ultra-short pulses (< 400 fs) that leave no thermal fingerprint on the contact lens, i.e. avoiding the creation of residual stresses and microstructural change in the material and thus preserving its properties/characteristics.<sup>19</sup> Fine features can be engraved onto thin substrates (10-100 μm), while still maintaining mechanical and material integrity (**Figure 1B**). They do not produce microcracks, recast layers or debris, as observed with CO<sub>2</sub> lasers (**Figure 1C**).<sup>19</sup> Femtosecond lasers are currently used for the fine machining of stents,<sup>20</sup> catheters, heart valves, polymer fibres and tubes.<sup>21, 22</sup> Recent studies also report on the use of femtosecond laser ablation to produce hierarchical, periodic structures<sup>23-27</sup> in optical crystals,<sup>28</sup> and to aid the synthesis of nanoparticles for medical application.<sup>22, 29, 30</sup>

Here, femtosecond laser inscription technology was applied to commercial contact lens devices. Multiple microfluidic elements (valves, resistors, multi-inlet geometries, splitters, reservoirs, sensing cavities and more complex geometries) were produced into contact lenses. Two applications of this technology are demonstrated, in the form of a tear volume sensor for dry eye disease, and a uric acid sensor to monitor gout disease progression from tears. This approach has

achieved the highest resolution (80  $\mu\text{m}$ ) observed thus far to produce microfluidic contact lenses in a single step. This work paves the way towards the incorporation of complex fluidic networks, and hence complex functionalities, within a single contact lens and in establishing femtosecond laser inscribed contact lenses as the pillar platform for monitoring both ocular and systemic health.

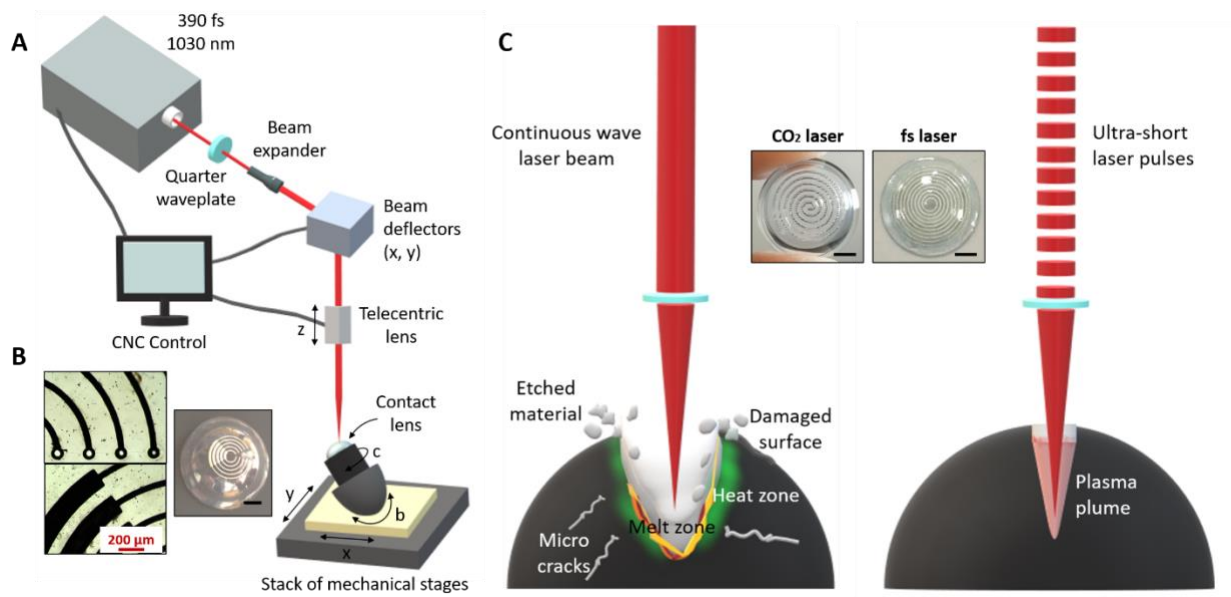


**Figure 1.** Femtosecond laser ablation. A) Schematic of the laser multi-axis processing setup. B) Examples of microstructures inscribed in contact lenses: micrographs of a micro-valve system (scale bar: 200  $\mu\text{m}$ ), photograph of an engraved contact lens (scale bar: 3 mm). C) Schematic comparing laser ablation performed with a long pulse laser beam (e.g. nanosecond and CW CO<sub>2</sub> lasers) and ultra-short laser pulses (femtosecond lasers). The insets show a contact lens engraved with each process, where the higher resolution obtained by ultra-short laser pulses is clearly visible. Scale bars: 3 mm.

## Results

Microfluidic elements and networks were engraved into commercial fluorosilicone acrylate commercial contact lenses, with a thickness of 120  $\mu\text{m}$ , using a 7-axis femtosecond laser

workstation as depicted in Figure 1A. Details on the components are presented in **Supplementary Figure S1**. This allowed to uniformly engrave each area of the sample, regardless of the curvature. The settings were optimized to yield features with a depth of 80-100  $\mu\text{m}$ , and microchannels with a base width of 100  $\mu\text{m}$ . Optimized parameters are primarily scanning speed, pulse energy, frequency, and 7-axis machining protocol.

Ultrafast laser ablation of polymethyl methacrylate (PMMA) has been explained by photochemical, photothermal, and photophysical models.<sup>31</sup> The photochemical model is based on PMMA direct bond breaking, which results in products such as CO, CO<sub>2</sub>, CH<sub>4</sub>, CH<sub>3</sub>OH, and HCOOCH<sub>3</sub>. The photothermal model considers thermal bond breaking induced by ultra-short laser pulses which induce the formation of PMMA monomers. The photophysical model includes both bond breaking processes happening simultaneously. The three main processes of photophysical laser-induced breakdown are the excitation of conduction band electrons through ionization, heating of conduction band electrons through irradiation of the dielectric, and plasma energy transfer to the lattice.<sup>32, 33</sup>

This is observable when looking at the roughness profiles of microchannels etched in contact lenses using a CO<sub>2</sub> or a femtosecond laser. Supplementary Figure S2 displays the surface topography, where a difference in both geometrical consistency and damaging of the surrounding material can be noticed (Figure S2A,B). In particular, the microchannel obtained using a femtosecond laser displayed higher uniformity in depth, higher geometrical confinement, and sharper edges. The roughness profile yielded empirical values of  $S_a(\text{CO}_2) = 10.7 \mu\text{m}$  and  $S_a(\text{fs}) = 3.4 \mu\text{m}$  (Figure S2C-F). The microfluidic geometries were designed such to be placed outside of the pupil area, to avoid visual impairment during wear. However, multi-inlet geometries were patterned towards the center to allow a better visualization in the context of this article. **Figure 2**

shows a computational evaluation on the impact of scanning speed and pulse energy on ablation depth and ablated mass (intended to be the amount of material (pg) etched away during laser writing), performed by the finite element method (FEM) and considering a pure photothermal process. **Figure 2A** displays the effect of gradually increasing the pulse energy while keeping a constant beam scanning speed of 10 mm/s and pulse frequency of 50 kHz. We can observe a linear behavior for pulse energy values from 20  $\mu\text{J}$  to 60  $\mu\text{J}$  (**Figure 2B**). A speed of 10 mm/s and pulse energy of 50  $\mu\text{J}$  yields an average ablation depth of 90  $\mu\text{m}$ . Similarly, as observed in **Figure 2C**, at a constant pulse energy of 50  $\mu\text{J}$  and average power of 2.5 W, an increase in velocity results in a lower ablation depth, going from 180  $\mu\text{m}$  at a speed of 6 mm/s to 40  $\mu\text{m}$  at a speed of 16 mm/s (**Figure 2D**). In the experiments, for all devices a speed of 10 mm/s and a pulse energy of 50  $\mu\text{J}$  were used. In the simulations, the pulse frequency was set to 50 kHz, the pulse duration to 390 fs, and beam spot diameter to 35  $\mu\text{m}$  at a wavelength of 1030 nm. Laser ablation computational results were obtained with a MATLAB model tailored to PMMA, a well-known material that most resembles the mechanical and physical properties of fluorosilicone acrylates.<sup>3</sup>

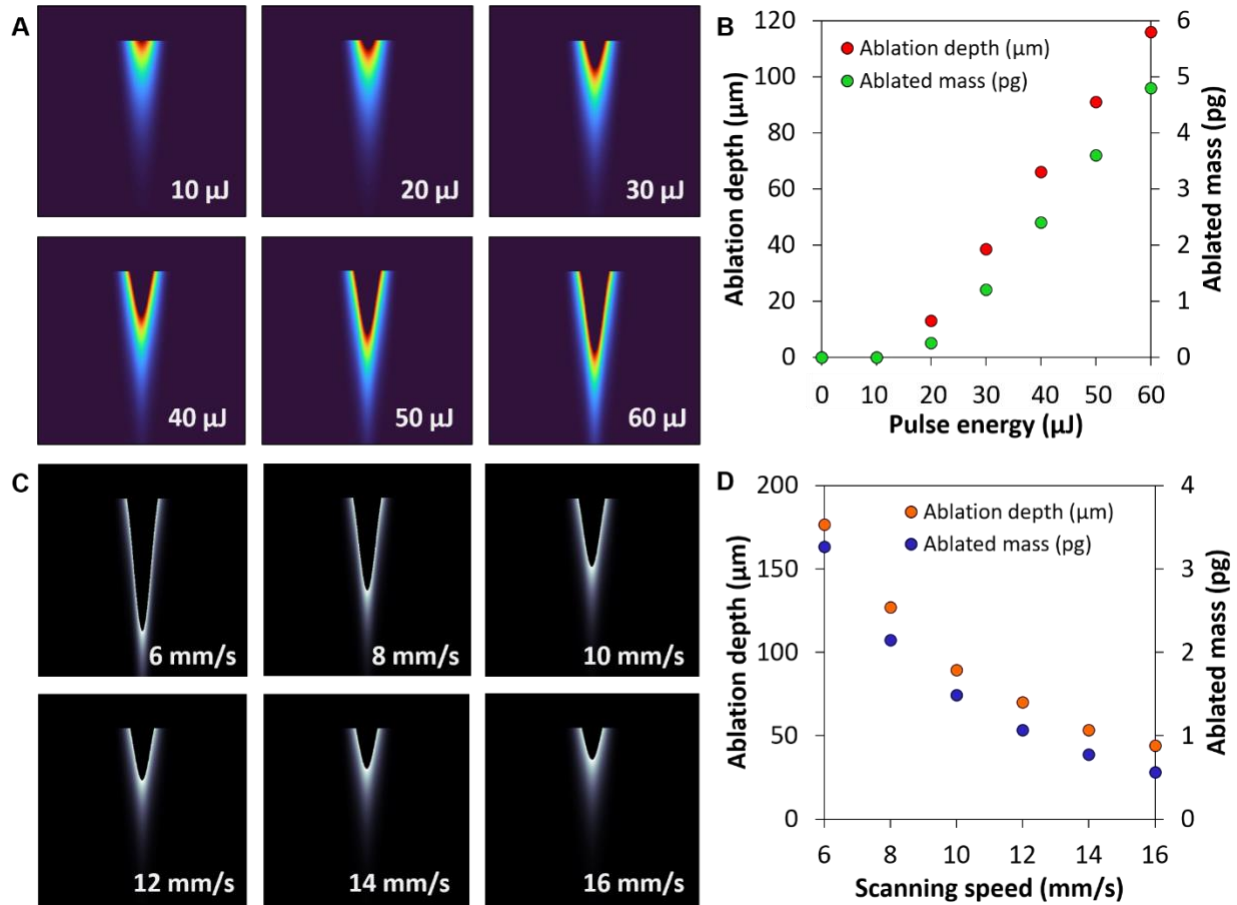


**Figure 2.** Computational evaluation of the laser ablation process by time-resolved FEM modelling. A-B) Influence of pulse energy (0-60  $\mu\text{J}$ ) on ablation depth and ablated mass of PMMA for a speed of 10 mm/s. C-D) Influence of beam scanning speed (6-16 mm/s) on ablation depth and mass for a laser power of 2.5 W.

**Figure 3** shows a set of valves engraved onto contact lenses. Microfluidic valves are used to adjust the flow velocity in certain areas of the channel. Photographs of the devices are showed in **Figure 3A**, namely a regular microchannel with a uniform width of 100  $\mu\text{m}$ , and the same channel with the addition of three different valve geometries, having width enlargements of the 100%, 200% and 300% (200  $\mu\text{m}$ , 300  $\mu\text{m}$  and 400  $\mu\text{m}$ , respectively), compared to the base channel. Micrographs of the valves are shown in **Figure 3B**. Geometrical details are presented in

**Supplementary Figure S3.** Prior to experimental flow evaluations, contact lenses were hydrophilized via oxygen plasma treatment (**Supplementary Figure S4**). A blue dye and a smartphone camera were used to evaluate the capillary filling time of each geometry, resulting in an average decrease of 0.25 s per 100% of channel enlargement (**Figure 3C**). The flow velocity profile within the same geometries was computed with the finite element method (**Figure 3D**). At time  $t = 0$  ms, all profiles appear dark blue (null velocity). At  $t = 0.5$  ms, the velocity profile reaches a value of 6.5 mm/s in the base channel, 4.0 mm/s in V1 (100%), 3.0 mm/s V2 (200%), and 2 mm/s in V3 (300%). Similarly, at  $t = 1$  ms, the base channel draws a velocity profile with an average of 7 mm/s, compared to 5 mm/s in V1, 3.5 mm/s in V2, and 3 mm/s in V3. The plots next to each set of figures display the cross-sectional velocity profile comparison between channel and valve in the four geometries at the three times of consideration (0 ms, 0.5 ms, 1 ms).

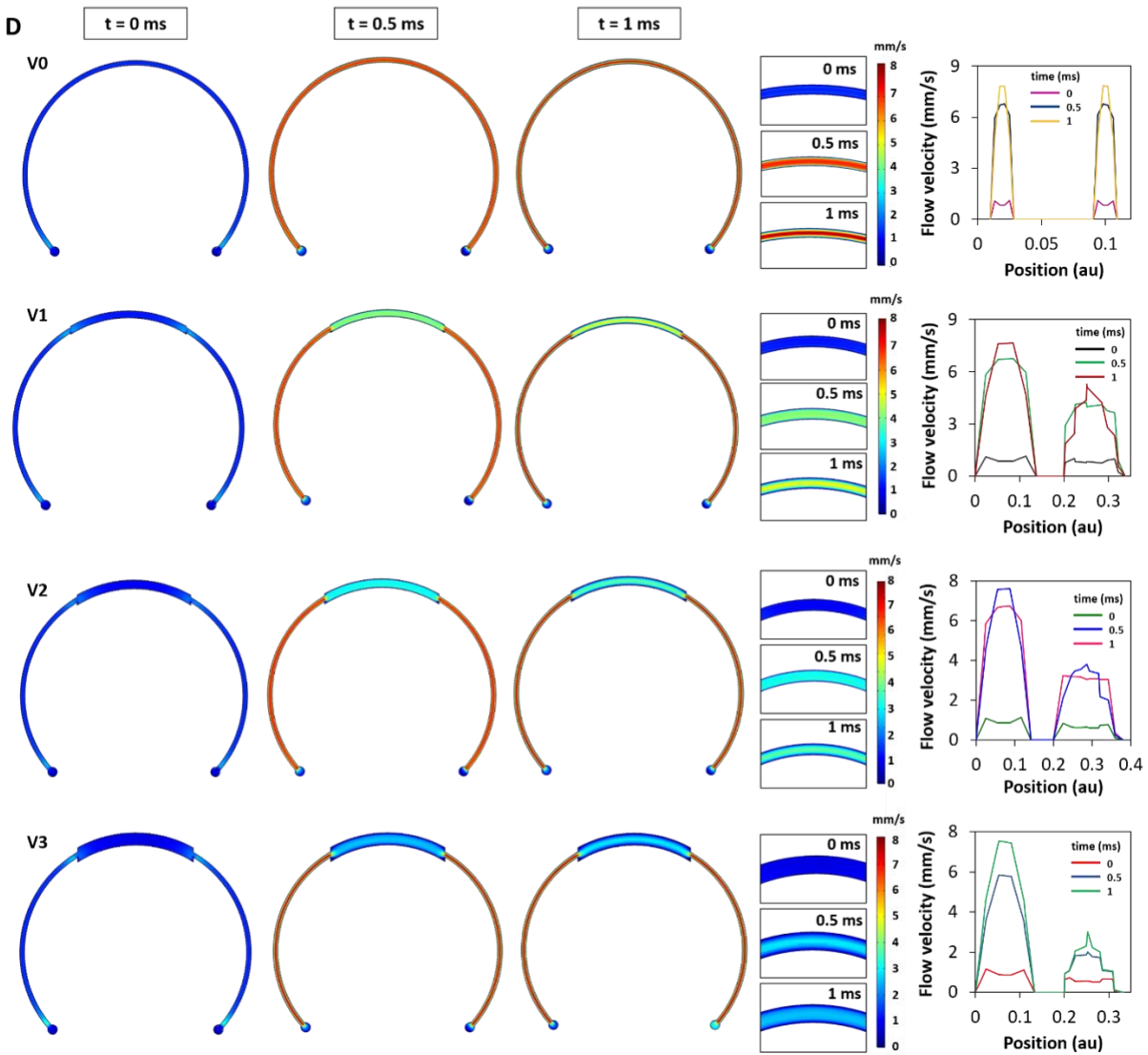
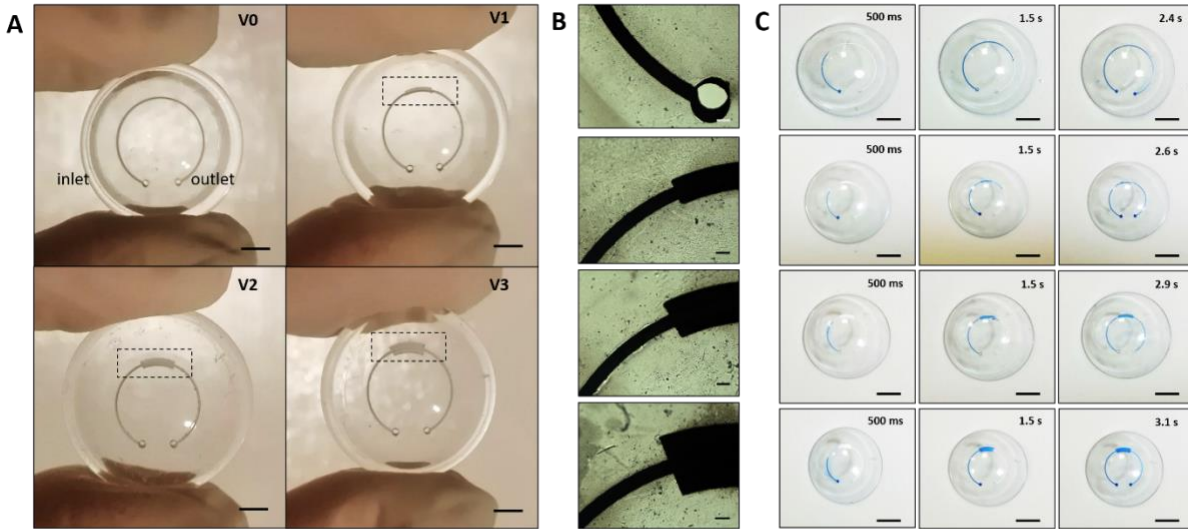


**Figure 3.** Flow valves engraved in contact lenses. A) Photographs of base channel V0 (constant thickness of 120  $\mu\text{m}$ ), V1 (100% enlargement), V2 (200% enlargement), and V3 (300% enlargement). Scale bars: 3 mm. B) Micrographs of flow valves: inlet, 100%, 200%, 300%. Scale bars: 100  $\mu\text{m}$ . C) Fluid flow within microfluidic contact lens valves. Scale bars: 5 mm. D) Computational fluid flow within valves.

**Figure 4** shows a set of resistors engraved in contact lenses. Microfluidic resistors are used to either reduce the fluid flow velocity in certain sections, or to decrease the overall velocity by increasing the total volume of the network, while keeping it confined to the same area. In this case, three types of resistors were compared. Photographs of the devices are shown in **Figure 4A**, named R1 to R3. R0 is the base channel, also shown for comparison. Micrographs of the resistors are shown in **Figure 4B**. Blue or green dyes were injected in the contact lenses via the inlet (concave side) using a PCV tube (diameter 0.5 mm) and a syringe, and a smartphone camera was used to capture the filling time (**Figure 4C**). It is observed that the fluid filled geometry R1 in 2.9 s, R2 in 3.2 s, R3 in 3.6 s, compared to the base channel which was filled in 2.4 s. This is explained by the gravity contribution. Overall, all geometries exhibited visible increased filling time compared to the base channel. This was also observed in computational studies (**Figure 4D**), where at  $t = 1$  ms all geometries reach velocities above 6.5 mm/s in correspondence of the resistors. However, at 0.5 ms the velocity profile is higher in R1, the resistor with the largest width. R2 and R3 register comparable profiles, with slightly lower velocities in R3. The plots next to each set of figures display the cross-sectional velocity profiles taken by drawing a horizontal line along the resistors, hence 4 peaks. Geometrical details are presented in **Supplementary Figure S5**.

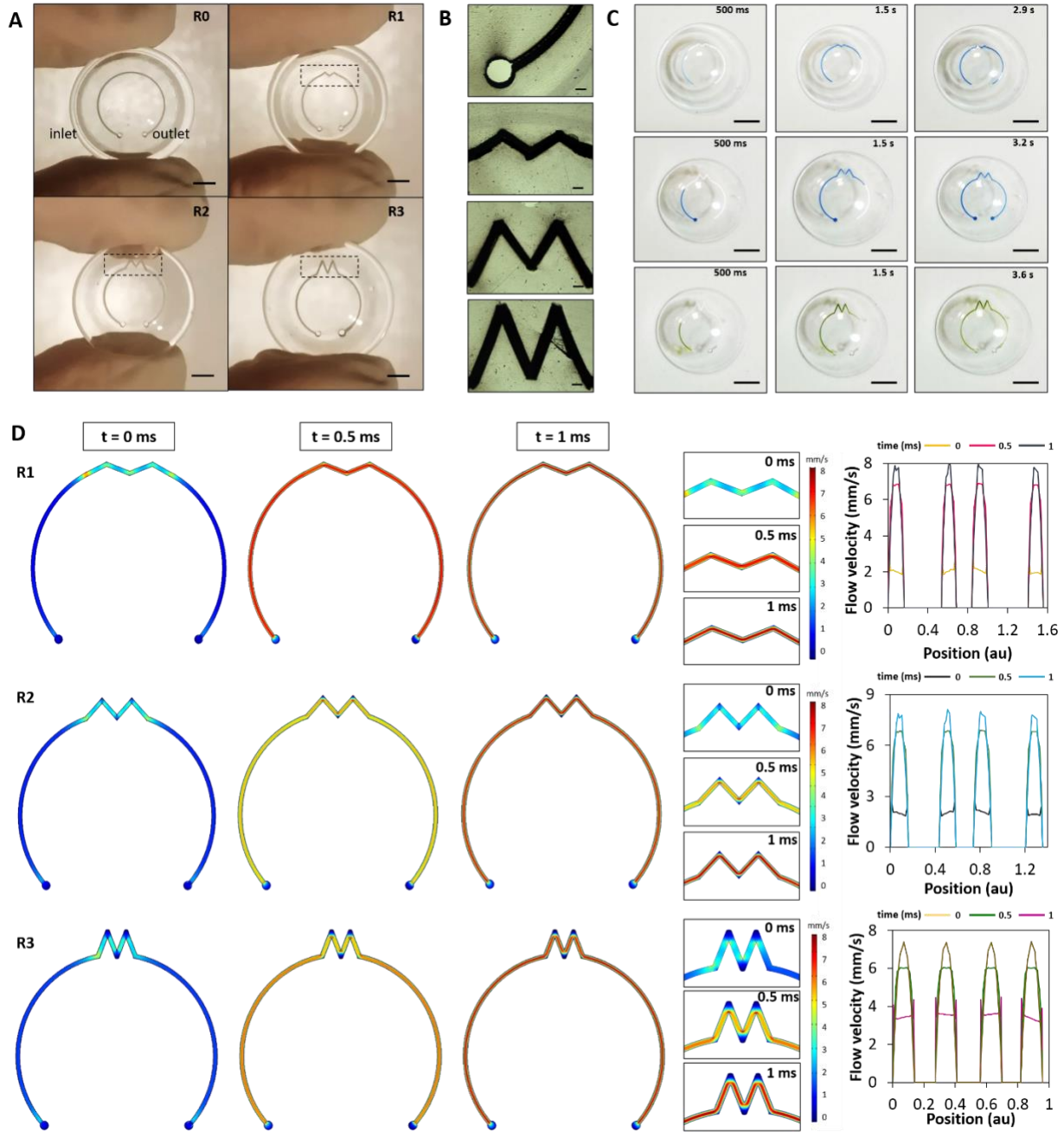


**Figure 4.** Flow resistors engraved in contact lenses. A) Photographs of base channel R0, R1 (wide resistor), R2 (standard resistor), and R3 (narrow resistor). Scale bars: 3 mm. B) Micrographs of flow resistors: inlet, wide, standard, narrow. Scale bars: 100  $\mu\text{m}$ . C) Fluid flow within microfluidic contact lens resistors. Scale bars: 5 mm. D) Computational fluid flow within resistors.

Multi-inlet geometries are highly used in microfluidics as the base platform to develop bespoke mixers for different scopes. They are a useful tool in sensing applications, where two solutions may need to be mixed before encountering tear fluid, or before interacting with a chemical sensor. In this framework, two multi-inlet geometries were fabricated on contact lenses (**Figure 5**). **Figure 5A** displays photographs of the multi-inlet geometries, namely the two-branched M1 and four-branched M2. Their micrographs are shown in **Figure 5B**. Blue and green dyes were injected in the contact lenses at the same time via the inlets, and a smartphone camera was used to capture the filling time (**Figure 5C**). It resulted that M1 had a total filling time of 1.7 s, lower than the one registered for the base channel (2.4 s), attributed to the gravity contribution and the presence of two inlet sources. M2 was filled in 2.3 s from four inlets. Computational studies were performed to evaluate the velocity profiles in such geometries (**Figure 5D**), yielding a higher velocity in the branches of M1 (12 mm/s at  $t = 1$  ms) than M2 (10 mm/s at  $t = 1$  ms). The plots next to each set of figures represent the velocity profile in the cross-section, traced by drawing a horizontal line along the inlet branches. Geometrical details are presented in **Supplementary Figure S6**.

Similarly, splitters are used in microfluidics to guide the flow towards different areas of the network. In contact lenses this is particularly interesting when multiplexing chemical sensors to detect multiple tear analytes in the same device. In fact, in the case of optical sensor (e.g. colorimetric, fluorescent) the fluid coming from the sensing area may be contaminated with sensing material. This can be prevented by devoting different microfluidic areas to different sensors. Here, two splitter geometries were fabricated on contact lenses. **Figure 5E** displays photographs of the splitters, namely the two-branched S1 and four-branched S2. Their micrographs are shown in **Figure 5F**. Blue and green dyes were injected in the contact lenses, and a smartphone camera was used to capture the filling time (**Figure 5G**). S1 had a total filling time of 2.1 s, again

lower than the one registered for the base channel (2.4 s), attributed to the gravity contribution. In S2, the four outlets were reached in 2.8 s. Computational studies were performed to evaluate the velocity profiles in splitter geometries (**Figure 5H**), yielding an average velocity profile of 3.8 mm/s at  $t = 1$  ms in the branches of S1. In S2, we observed higher velocity profiles in the inner branches (1.3 mm/s at  $t = 1$  ms), compared to the outer branches (1.1 mm/s at  $t = 1$  ms). In both cases, the highest velocity profiles were found to be near the inlet, right before splitting (7.5 mm/s at  $t = 0.5$  ms). The plots next to each set of figures represent the velocity profile in the cross-section, traced by drawing a horizontal line along the outlet branches. Geometrical details are presented in **Supplementary Figure S7**.

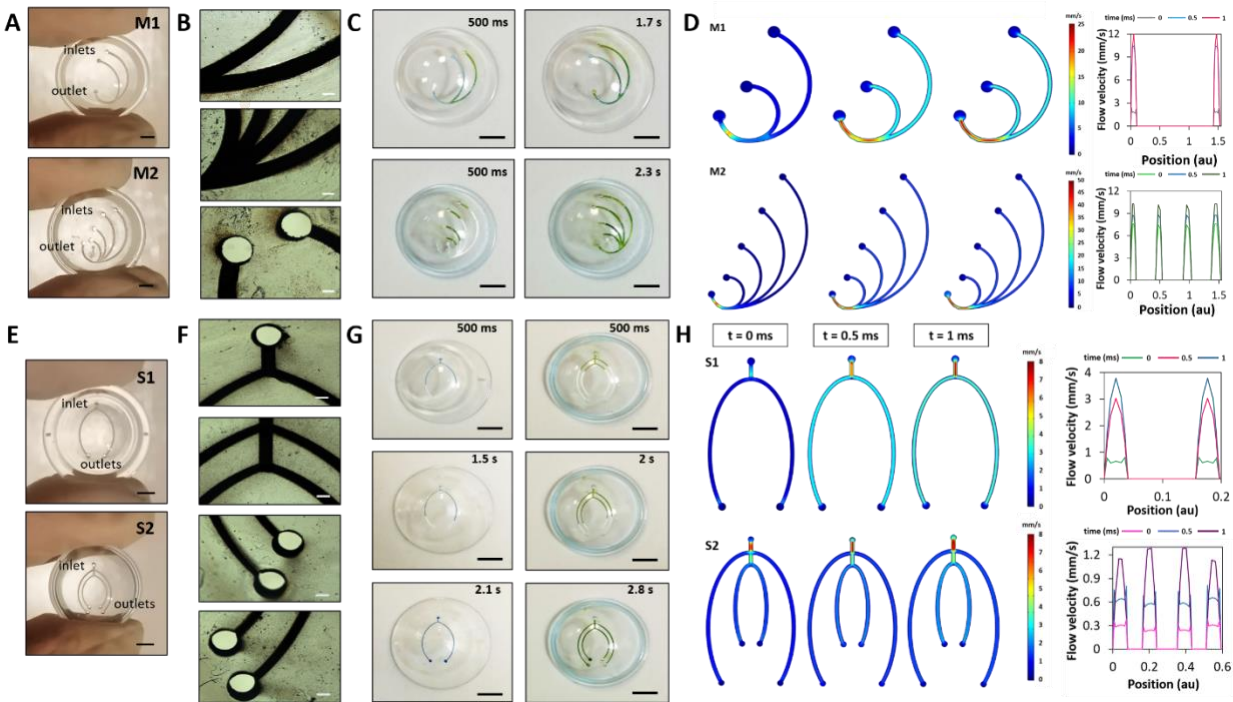


**Figure 5.** Flow multi-inlet geometries and splitters engraved in contact lenses. A) Photographs of microfluidic multi-inlet geometries M1 (two inlets, one outlet), and M2 (four inlets, one outlet). Scale bars: 3 mm. B) Micrographs of fluid multi-inlet channels: two-branched, four-branched, inlet-outlet. Scale bars: 50 μm. C) Fluid flow within microfluidic multi-inlet channels. Scale bars: 5 mm. D) Computational fluid flow within multi-inlet channels. E) Photographs of microfluidic splitters S1 (one inlet, two outlets), and S2 (one inlet, four outlets). Scale bars: 3 mm. F)

Micrographs of fluid splitters: two-branched, four-branched, outlets (right side), outlets (left side). Scale bars: 150  $\mu\text{m}$ . C) Fluid flow within microfluidic multi-inlet channels. Scale bars: 4 mm. D) Computational fluid flow within multi-inlet channels.

Precisely inscribing microfluidic elements in contact lenses opens the way to a broad range of applications. These can be achieved by combining multiple elements to create a microfluidic network that performs a specific function. Microchannels on their own can already provide a smart alternative to current methods. On the other end, they may constitute the pillar platform to capitalize on for theranostic applications, by integrating sensors, drug delivery mechanisms, or both.

Here, two possible applications in the context of tear fluid monitoring are discussed. Both are addressed in the closed configuration, where the inlet is patterned as a hole in the concave side of the bottom lens, in direct contact with the ocular surface, and the outlet is a hole etched from the convex side in the top lens. Closed configurations were only presented for the applications, where a full device is a must. On the contrary, microfluidic elements were assessed earlier in this article in an open configuration (both inlets and outlets engraved as holes in a single lens). In fact, in those cases the scope was to evaluate the “absolute” impact of valves and resistors on the flow velocity, and neither of them has an application on their own.

A tear fluid volume wearable sensor based purely on microfluidics may be an alternative to the Schirmer’s test (**Figure 6**). A spiral microfluidic channel was engraved on a contact lens (**Figure 6A**). Micrographs of the channel are shown in **Figure 6B**. The spiral features an inlet in the center, around the pupil area. The outlet is placed on the outer turn of the spiral. In this case, the outlet

acts as a pressure regulator more than just strictly as an outlet. In fact, the spiral can host a tear volume of 30  $\mu\text{L}$ , whilst the total average tear volume on the anterior eye amounts to 5 to 7  $\mu\text{L}$ . Computational evaluations suggest that the velocity profile is uniform along the spiral (**Figure 6C**). To close the microfluidic channel, a lab-made PDMS contact lens was fabricated by replica molding from a curved contact lens mold (**Figure 6D**), and chemically bonded to the engraved lens, based on oxygen plasma treatment, silanization with (3-Aminopropyl)triethoxysilane (APTES) and (3-Glycidyloxypropyl)triethoxysilane (GPTES), and direct contact, as shown in **Figure 6E**<sup>34</sup>. In an industrial setting, this process could be automated by using a thinner rigid contact lens as a top layer. The method currently used to assess the tear volume in dry eye patients is the Schirmer's test.<sup>3</sup> This consists on inserting a paper strip in the lower eyelid of the patient for 5 minutes, followed by visual readout of the wetted area to semi-quantitatively assess the tear fluid production (**Figure 6F**). This process is painful, adds up contamination risks, and induces local irritation which results in tear overflow and false negative results. The spiral lens may be a promising alternative. **Figure 6G** displays the proposed use of such device. Upon inserting the lens, the tear flows from the channel inlet, placed on the concave side of the lens, through the spiral. The contact lens was exposed to 3  $\mu\text{L}$  and 8  $\mu\text{L}$  of artificial tears, respectively. The volume of the tear film may be assessed by visual method, based on the wetted spiral area after 10 s.

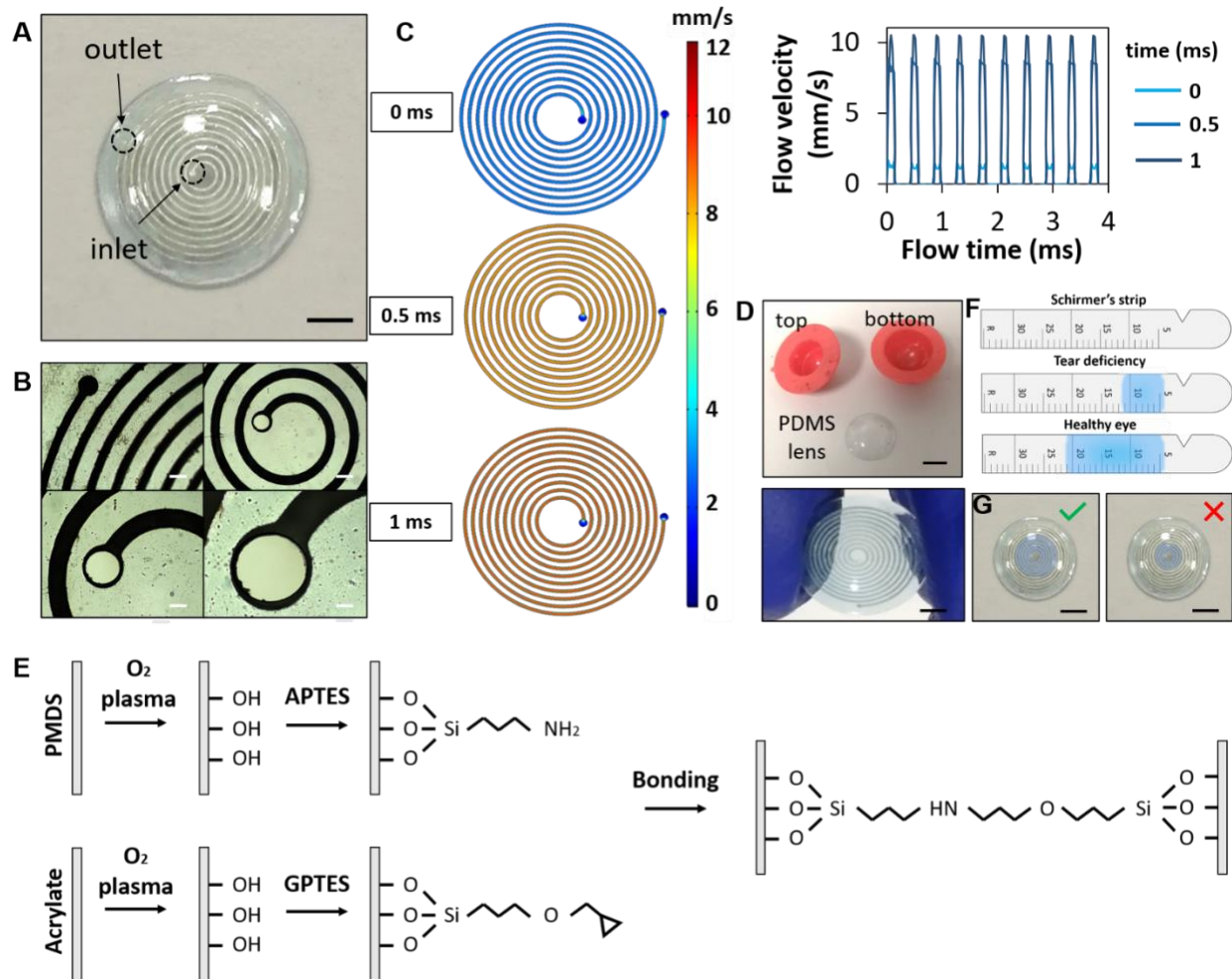


**Figure 6.** Microfluidic tear volume sensor. A) Photographs of the volume sensor (spiral channel engraved on a contact lens). Scale bar: 5 mm. B) Micrographs of the spiral channel. Scale bars: 150  $\mu\text{m}$ . C) Computational velocity profile within the spiral lens. D) Contact lens sensor: PDMS lens fabricated in a plastic mold, and bonded to the spiral acrylic lens. Scale bars: 1 cm (top), 3 mm (bottom). E) PDMS-to-acrylic chemical bonding process. F) Working principle of the Schirmer's test to assess tear fluid volume. G) Visual readout of fluid volume from a microfluidic contact lens, based on the wetted spiral area. Scale bar: 5 mm.

The tear volume sensor may be re-used. After sampling the tear fluid from a patient, the liquid may be collected using a capillary tube and stored in a sterile container or thrown away if the lens was to be used to evaluate the tear fluid production. Following that, the lens may be disinfected,

dried and re-used. A cleaning protocol would need to be tailored for this specific need. The tear uric acid sensor is disposable and meant for one-off measurements.

Another application is presented in **Figure 7**. Here, a microfluidic channel featuring an inlet, sensing area, fluidic valve and a reservoir is demonstrated for the detection of uric acid on-eye (**Figure 7A,B**). Uric acid is an extensively known biomarker for gout disease progression, as well as to monitor the antioxidant status in the eye.<sup>35-37</sup> The tear flows from the inlet to the sensing area, where the colorimetric uric acid sensor is embedded. From the sensing area, the fluid encounters a valve with an enlargement of the 300% compared to the base channel, which decreases the flow velocity of the 60%, until reaching a reservoir, where the fluid velocity stops (**Figure 7C**). Computational evaluations show that there is no backflow from the reservoir to the valve, nor from the valve to the sensing area (**Figure 7D**).

The uric acid sensor was based on uricase and horseradish peroxidase (HRP). In the presence of oxygen, water and uricase, uric acid is converted into 5-hydroxyisourate and hydrogen peroxide. 5-hydroxyisourate further reacts with water to produce allantoin and CO<sub>2</sub>. Hydrogen peroxide, in the presence of HRP, reacts with 4-aminoantipyrine and with N-Ethyl-N-(2-hydroxy-3-sulfopropyl)-3,5-dimethoxyaniline (MAOS) to produce a blue dye. The amount of blue dye produced is proportional to the amount of hydrogen peroxide obtained by reaction of uric acid, yielding a color scale proportional to uric acid concentration (**Figure 7E**). The reflection spectra of the uric acid sensor at concentrations of 0, 50, 100, 150, 200 and 250 mg/L are shown in **Figure 7F**. The calibration curve is displayed in **Figure 7G**, from which a sensitivity of 16 mg/L was calculated. The sensor is embedded in the sensing cavity etched in the contact lens, and the color of the sensor could be readout using a smartphone app (Color Grab) to assess the red, green and blue (RGB) composition, and correlated to a discrete concentration value in the range 0-250 mg/L



**Figure 7.** Microfluidic contact lens as a tear uric acid sensor. A) Photograph of the engraved contact lens, featuring inlet, channel, sensing area, flow valve, and reservoir. Scale bar: 3 mm. B) Micrographs of the microfluidic areas. Scale bars: 400  $\mu\text{m}$ . C) Velocity profile along the contact lens: the flow velocity is at its maximum within the channel section, decreases at the sensing area and stops in correspondence of the reservoir. D) Computational velocity profile within the geometry. E) Sensing reaction. Uric acid is converted into hydrogen peroxide, which further reacts with 4-AMP to produce a blue dye. Insets show the color change of the sensor in the concentration range 0-250 mg/L. F) Reflection spectra of the uric acid sensor in the concentration range 0-250 mg/L. G) Calibration curve of the sensor. H) Uric acid sensor embedded in a contact lens and placed on an eye model where artificial tear flows. The color is captured with a smartphone camera. Scale bars (left, right, bottom): 3 mm, 7 mm, 1.5 cm. I) RGB color characterization of the uric acid sensor.

## Materials and Methods

**Materials.** Rigid contact lenses (Boston XO) were obtained from Bausch & Lomb, Canada. Sylgard 184 silicone elastomer kit (1:10) was purchased from Dow Corning, USA. (3-Aminopropyl)triethoxysilane (APTES), (3-Glycidyloxypropyl)triethoxysilane (GPTES), uric acid, D-(+)-glucose (99.5%), protein standard (200 mg/mL), boric acid, ethylenediaminetetraacetic acid (EDTA), 10% triton X-100, sodium borate, isopropanol (IPA) and phosphate buffered saline (PBS) were purchased from Sigma-Aldrich, UK and used without further purification. Uric acid colorimetric assays were purchased online from Health Mate, UK. Green and blue food coloring dyes (Waitrose Essentials) were purchased from Waitrose & Partners, UK. Systane artificial tears were purchased from Boots Ltd., UK and modified as needed.

**Equipment.** A LS4 LASEA workstation was used that integrates a femtosecond laser source (YUJA from Amplitude Systemes) with the following technical characteristics: 10W average power, 100  $\mu\text{J}$  maximum pulse energy, 390 fs pulse duration, 2 MHz maximum repetition rate,

1030 nm center wavelength and beam quality  $M2 > 1.2$ . The beam delivery system was equipped with a X-Y beam deflectors, synchronized with a stack of mechanical stages (3 linear stages X-Y-Z and 2 rotary stages B, C).

Oxygen plasma system Atto Model 4 with 40 kHz 200 W generator (Diener electronic GmbH + Co. KG, Germany), Smartphone camera (photo 12 MP, f/2.2, 1/2.8", 1.25 $\mu$ m, PDAF; video 1080p@30fps), FLAME-S-VIS-NIR-ES Spectrometer Assembly 350-1000nm (Ocean Insight, USA), pH meter FiveEasy F20 (Mettler Toledo, USA), Pioneer PX 323/E Precision Balance (Ohaus, USA), Vortex Mixer (Fisherbrand, UK), Visible Light Source HL-2000-HP-FHSA 20W (Ocean Optics, USA), Leica DM2700 P Upright Microscope (Leica Microsystems GmbH, Germany), Contact angle measurements: VHX-1000 digital microscope (Keyence Corporation, Japan) with a custom 3D printed fixture for dispensing deionized water droplets with a 10  $\mu$ l pipette (Eppendorf, Germany).

**Software.** MATLAB R2020B (MathWorks, USA), COMSOL Multiphysics v5.3a (Comol Inc., Sweden), Color Grab application (Loomatix Ltd., ) installed on a Huawei P10 Lite (Huawei Technologies Co., Ltd, China) running Android 10.0 mobile operating system (Google LLC, USA), contact angle measurements using the contact angle measurement plug-in in ImageJ. The GibbsCAM software was used to programme the multiaxis laser processing.

**Laser ablation simulations.** Femtosecond laser ablation of PMMA was simulated using time-domain FEM modeling, assuming a purely photothermal process, described by the heat equation:

$$Q = \frac{\partial U}{\partial t} - D \nabla^2 U \text{ (Eq. 1)}$$

where  $Q$  is the heat transferred from the laser and to PMMA and  $D$  the thermal diffusivity of PMMA. Beam spot diameter, step over, frequency, wavelength, and pulse duration were set to 35

$\mu\text{m}$ , 20  $\mu\text{m}$ , 50 kHz, 1030 nm and 390 fs, respectively. Beam scanning speed and pulse energy were set in the range 6-16 mm/s and 0-60  $\mu\text{J}$ , respectively, to estimate their impact on ablation depth and ablated mass of PMMA. The properties of PMMA were obtained from the literature<sup>38</sup>: thermal capacity (1418 J kg<sup>-1</sup> K<sup>-1</sup>), density (1180 kg m<sup>-3</sup>), and thermal diffusivity (0.115e-6 m<sup>2</sup> s<sup>-1</sup>).

**Femtosecond laser micro-processing of contact lenses.** A fractional factorial design was conducted to optimize laser parameters, yielding optimized values of 50 kHz (pulse frequency), 50  $\mu\text{J}$  (pulse energy), 10 mm/s (scanning speed) and 20  $\mu\text{m}$  (step over). To achieve a uniform geometry of the micro-features regardless of the contact lens curvature, the laser beam focused was continuously monitored and kept normal to the surface. For a freeform surface like a contact lens this was achieved by implementing two rotary stages and X-Y-Z linear stages, synchronized with X and Y beam deflectors.

**Microfluidic simulations.** Microfluidic 2D geometries were designed on COMSOL and tear flow was evaluated under laminar regime. The solid material was defined as PMMA and assigned to the microchannel area. The liquid material was customized to reproduce the aqueous tear film by defining an incompressible Newtonian fluid with viscosity  $\mu = 1.3 \times 10^{-3}$  Pa s, surface tension  $\sigma = 0.045$  N m<sup>-1</sup>, thermal conductivity  $k = 0.68$  W m<sup>-1</sup> K<sup>-1</sup>, density  $\rho = 103$  kg m<sup>-3</sup>, and characteristic speed  $U_0 = 5 \times 10^{-3}$  m s<sup>-1</sup>.<sup>39</sup> An incompressible, single-phase fluid assumes that temperature variations in the flow are small, which means that the density is constant, described by the continuity and the momentum equations:

$$\rho \nabla \cdot \mathbf{u} = 0 \text{ (Eq. 2)}$$

$$\rho \frac{\partial \mathbf{u}}{\partial t} + \rho(\mathbf{u} \cdot \nabla)\mathbf{u} = \nabla \cdot [-p\mathbf{I} + \mu(\nabla\mathbf{u} + (\nabla\mathbf{u})^T)] + \mathbf{F} \text{ (Eq. 3)}$$

Initial values for pressure and velocity were set to zero. At the microchannel walls, the equation was solved with an initial  $\mathbf{u} = 0$ , with “no slip” as the boundary condition. At the inlet, the equation was solved for  $\mathbf{u} = -U_0\mathbf{n}$  as the boundary condition, with  $U_0 = 0.1 \mu\text{m s}^{-1}$ . The time-dependent flows were computed for the interval (0:0.1:1) ms. The same constraints at the inlet and outlet were applied in all geometries.

**Flow characterization.** Flow experiments were conducted by injecting 10  $\mu\text{L}$  of dye via the inlet of the microchannels using a PVC tube with a diameter of 0.5 mm and connected to a liquid dispenser. The flow was recorded with a smartphone camera.

**Hydrophilization of contact lenses.** Contact lenses were  $\text{O}_2$  plasma treated for 1 min at full power (200 W). During the pumping down period the pressure was set to 0.07 mbar. The  $\text{O}_2$  gas supply was set to 5 min at a gas flow of 100% and a process pressure of 0.2 mbar.

**Preparation of PDMS contact lenses.** PDMS was obtained by mixing the elastomer pre-polymer and curing agent in a 10:1 weight ratio, followed by 2 h degassing at ambient temperature and manual removal of bubbles by exerting air flow using a pipette. 100  $\mu\text{L}$  of the uncured mixture was then poured into the contact lens mold and cured on a hot plate at 80° C for 15 minutes. The lenses were then removed from the mold, rinsed in isopropanol, and blow dried.

**Preparation of uric acid buffer solutions.** Uric acid has a low solubility in water, but it can be dissolved in borate buffer, NaOH and DI water. First, the borate buffer solution was prepared by dissolving boric acid (6.2 g), sodium borate (9.5 g) and EDTA (1.2 g) in 10% Triton X-100 (400  $\mu\text{L}$ ) and deionized water (200 mL), adjusting to a pH of 8.5 with NaOH. The uric acid diluent

solution was further obtained by mixing deionized water (150 mL) with borate buffer storage solution (8 mL), adjusting to a pH of 8.5 with NaOH. Uric acid was then diluted in the diluent solution to yield concentrations of 0, 50, 100, 150, 200, 250 mg/L. Uric acid buffer solutions were then mixed with Systane artificial tears and the pH was adjusted to 7.0 using tris buffers.

**Characterization of uric acid sensors.** Uric acid paper sensors were exposed to artificial tears containing uric acid in the concentration range 0-250 mg/L, at steps of 50 mg/L. Their colorimetric response was imaged with a smartphone camera placed at normal incidence at an ambient lighting of 250 lux (lx), monitored with Photometer PRO app, and the color was readout using Color Grab app. The reflection spectra and related calibration curve were acquired using a reflection setup consisting on a bifurcated optical fiber connected to a spectrometer and a light source, taking as a background reference the spectra obtained by irradiating a black-colored paper sensor made of the same material.

## **Conclusions**

Femtosecond laser ablation is a simple and effective method to inscribe fine microfluidic structures into rigid contact lenses. It overcomes the limitations encountered with longer pulse lasers, i.e. nanosecond and continuous wave (CW) CO<sub>2</sub> lasers. When designing microfluidic contact lenses, a crucial parameter to consider is the analysis time, hence the wearing time, to avoid tear overflow and, where present, leakage of the sensing materials. In this context, multiple microfluidic elements were demonstrated to provide a tool of playing with filling time (e.g. fluidic valves and resistors) and waste tears collection systems (e.g. reservoirs). The integration of colorimetric sensor was demonstrated in the mm range to allow an easier visualization with a smartphone

camera. However, the sensing area may be scaled down to the  $\mu\text{m}$  range when designing sensors based on a different optical mechanism (e.g. fluorescence), coupled to a smartphone-compatible readout device. Microfluidic contact lenses are a promising alternative to current sampling and screening methods in ophthalmology, offering the possibility to sample the tear fluid with a sterile method, as well as integrating complex fluidic networks to continuously monitor the tear fluid directly on-eye. Such devices may find application in ocular theranostics, by incorporating sensing technologies, drug delivery mechanisms, or both.

### **Acknowledgements**

The authors would like to acknowledge the support of LASEA SA, Belgium within the framework of the ESIF project “Smart Factory Hub” (SmartFub). R. M. acknowledges the University of Birmingham, UK for funding.

### AUTHOR INFORMATION

#### **Corresponding Author**

[\\*rosalia.moreddu@iit.it](mailto:*rosalia.moreddu@iit.it)

#### **Author Contributions**

R.M. and A.K.Y. conceived the idea. R.M. designed the experiments, designed the microfluidic networks, performed laser ablation simulations and CFD simulations, conducted imaging and microfluidic flow experiments, and wrote the manuscript. V. N. fabricated microfluidic networks into contact lenses. P. K. performed oxygen plasma treatment of contact lenses, and contact angle measurements. D. V., A. K. Y. and S. D. provided funding and intellectual contributions.

### **References**

1. The World Health Organization, Eye care, vision care, vision impairment and blindness. [https://www.who.int/health-topics/blindness-and-vision-loss#tab=tab\\_1](https://www.who.int/health-topics/blindness-and-vision-loss#tab=tab_1). Accessed in March 2021.
2. S. Hagan, E. Martin, A. Enríquez de Salamanca, Tear fluid biomarkers in ocular and systemic disease: potential use for predictive, preventive and personalised medicine. *EMPA Journal* **2016**, 7 (1), 15.
3. R. Moreddu, D. Vigolo, A. K. Yetisen, Contact Lens Technology: From Fundamentals to Applications. *Advanced Healthcare Materials* **2019**, 8 (15), 1900368.
4. M. Senchyna, M. B. Wax, Quantitative assessment of tear production: A review of methods and utility in dry eye drug discovery. *Journal of Ocular Biology, Diseases, and Informatics* **2008**, 1, 1–6.
5. P. Versura, M. Frigato, M. Cellini, R. Mulè, N. Malavolta, E. C. Campos, Diagnostic performance of tear function tests in Sjogren's syndrome patients. *Eye* **2007**, 21, 229–237.
6. N. Li, X. G. Deng, M. F. He, Comparison of the Schirmer I test with and without topical anesthesia for diagnosing dry eye. *International Journal of Ophthalmology* **2012**, 5 (4), 478–481.
7. R. Moreddu, J. S. Wolffsohn, D. Vigolo, A. K. Yetisen, Laser-inscribed contact lens sensors for the detection of analytes in the tear fluid. *Sensors and Actuators B: Chemical* **2020**, 317, 128183.
8. R. Moreddu, M. Elsherif, H. Adams, D. Moschou, M. F. Cordeiro, J. S. Wolffsohn, D. Vigolo, H. Butt, J. M. Cooper, A. K. Yetisen, Integration of paper microfluidic sensors into contact lenses for tear fluid analysis. *Lab on a Chip* **2020**, 20, 3970-3979.
9. R. S. Riaz, M. Elsherif, R. Moreddu, I. Rashid, M. U. Hassan, A. K. Yetisen, H. Butt, Anthocyanin-functionalized contact lens sensors for ocular pH monitoring. *ACS Omega* **2019**, 4 (26), 21792–21798.
10. Y. Chen, S. Zhang, Q. Cui, J. Ni, X. Wang, X. Cheng, H. Alem, P. Tebon, C. Xu, C. Guo, R. Nasiri, R. Moreddu, A. K. Yetisen, S. Ahadian, N. Ashammakhi, S. Emaminejad, V. Jucaud, M. R. Dokmeci, A. Khademhosseini, Microengineered poly(HEMA) hydrogels for wearable contact lens biosensing. *Lab on a Chip* **2020**, 20, 4205-4214.
11. N. M. Farandos, A. K. Yetisen, M. J. Monteiro, C. R. Lowe, S. H. Yun, Contact lens sensors in ocular diagnostics. *Advanced Healthcare Materials* **2015**, 4 (6), 792-810.
12. R. Moreddu, M. Elsherif, H. Butt, D. Vigolo, A. K. Yetisen, Contact lenses for continuous ocular temperature monitoring. *RSC Advances* **2019**, 9, 11433-11442.
13. D. H. Keum, S. K. Kim, J. Koo, G. H. Lee, C. Jeon, J. W. Mok, B. H. Mun, K. J. Lee, E. Kamrani, C. K. Joo, S. Shin, J. Y. Sim, D. Myung, S. H. Yun, Z. Bao, S. K. Hahn, Wireless smart contact lens for diabetic diagnosis and therapy. *Science Advances* **2020**, 6 (17), 3252.
14. J. Kim, E. Cha, J. U. Park, Recent Advances in Smart Contact Lenses. *Advanced Materials Technologies* **2019**, 5 (1), 1900728.
15. M. Ku, J. Kim, J. E. Won, W. Kang, Y. G. Park, J. Park, J. H. Lee, J. Cheon, H. H. Lee, J. U. Park, Smart, soft contact lens for wireless immunosensing of cortisol. *Science Advances* **2020**, 6 (28), 2891.
16. S. Kim, H. J. Jeon, S. Park, D. Y. Lee, E. Chung, Tear Glucose Measurement by Reflectance Spectrum of a Nanoparticle Embedded Contact Lens. *Scientific Reports* **2020**, 10, 8254.
17. Y. Wang, Q. Zhao, X. Du, Structurally coloured contact lens sensor for point-of-care ophthalmic health monitoring. *Journal of Materials Chemistry B* **2020**, 8, 3519-3526.

18. N. Jiang, Y. Montelongo, H. Butt, A. K. Yetisen, Microfluidic contact lenses. *Small* **2018**, *14*, 1704363.
19. B. Guo, J. Sun, Y. Hua, N. Zhan, J. Jia, K. Chu, Femtosecond Laser Micro/Nano-manufacturing: Theories, Measurements, Methods, and Applications. *Nanomanufacturing and Metrology* **2020**, *3*, 26–67.
20. C. H. Hung, F. Y. Chang, Curve micromachining on the edges of nitinol biliary stent by ultrashort pulses laser. *Optics & Laser Technology* **2017**, *90*, 1-6.
21. A. Tavangara, B. Tan, K. Venkatakrishnana, Synthesis of bio-functionalized three-dimensional titania nanofibrous structures using femtosecond laser ablation. *Acta Biomaterialia* **2011**, *7* (6), 2726-2732.
22. D. F. Farson, H. W. Choi, B. Zimmerman, J. K. Steach, J. J. Chalmers, S. V. Olesik, L. J. Lee, Femtosecond laser micromachining of dielectric materials for biomedical applications. *Journal of Micromechanics and Microengineering* *18* (3), 35020.
23. H. Liu, W. Lin, Z. Lin, L. Ji, M. Hong, Self-Organized Periodic Microholes Array Formation on Aluminum Surface via Femtosecond Laser Ablation Induced Incubation Effect. *Advanced Functional Materials* **2019**, *29* (42), 1903576.
24. Y. Xu, L. Yan, X. Li, H. Xu, Fabrication of transition metal dichalcogenides quantum dots based on femtosecond laser ablation. *Scientific Reports* **2019**, *9*, 2931.
25. M. Keshavarz, P. Kassanos, B. Tan, K. Venkatakrishnan, Metal-oxide surface-enhanced Raman biosensor template towards point-of-care EGFR detection and cancer diagnostics. *Nanoscale Horizons* **2020**, *5*, 294-307.
26. M. Keshavarz, A. K. M. Rezaul Haque Chowdhury, P. Kassanos, B. Tan, K. Venkatakrishnan, Self-assembled N-doped Q-dot carbon nanostructures as a SERS-active biosensor with selective therapeutic functionality. *Sensors and Actuators B: Chemical* **2020**, *323*, 128703.
27. D. S. Zhang, K. Sugioka, Hierarchical microstructures with high spatial frequency laser induced periodic surface structures possessing different orientations created by femtosecond laser ablation of silicon in liquids. *Opto-Electronics Advances* **2019**, *2*, 190002.
28. Y. C. Jia, S. X. Wang, F. Chen, Femtosecond laser direct writing of flexibly configured waveguide geometries in optical crystals: fabrication and application. *Opto-Electronics Advances* **2020**, *3*, 190042.
29. M. Dhanunjaya, C. Byram, V. S. Vendamani, S. V. Rao, A. P. Pathak, S. N. Rao, Hafnium oxide nanoparticles fabricated by femtosecond laser ablation in water. *Applied Physics A* **2019**, *125*, 74.
30. M. G. John, K. M. Tibbetts, One-step femtosecond laser ablation synthesis of sub-3 nm gold nanoparticles stabilized by silica. *Applied Surface Science* **2019**, *475*, 1048-1057.
31. S. R. Cain, A photothermal model for polymer ablation: chemical modification *Journal of Physical Chemistry*. *Journal of Physical Chemistry* **1993**, *97*, 051902.
32. R.R. Gattass, E. Mazur, Femtosecond laser micromachining in transparent materials. *Nature Photonics* **2008**, *2*, 219-225.
33. M. Li, S. Menon, J. P. Nibarger, G. N. Gibson, Ultrafast electron dynamics in femtosecond optical breakdown of dielectrics. *Physical Review Letters* **1999**, *82* (11), 2394–2397.
34. L. Tanga, N. Y. Lee, A facile route for irreversible bonding of plastic-PDMS hybrid microdevices at room temperature. *Lab on a Chip* **2010**, (10), 1274-1280.

35. M. Park, H. Jung, Y. Jeong, K. H. Jeong, Plasmonic Schirmer Strip for Human Tear-Based Gouty Arthritis Diagnosis Using Surface-Enhanced Raman Scattering. *ACS Nano* **2017**, *11* (1), 438-443.
36. E. F. Gabriel, P. T. Garcia, T. M. Cardoso, F. M. Lopes, F. T. Martinsa, W. K. Coltro, Highly sensitive colorimetric detection of glucose and uric acid in biological fluids using chitosan-modified paper microfluidic devices. *Analyst* **2016**, *141*, 4749-4756.
37. J. Horwath-Winter, S. Kirchengast, A. Meinitzer, C. Wachswender, C. Faschinger, O. Schmut, Determination of uric acid concentrations in human tear fluid, aqueous humour and serum. *Acta Ophthalmologica* **2009**, *87* (2), 188-192.
38. Azon Materials, <https://www.azom.com/article.aspx?ArticleID=788>. Accessed in March 2021.
39. L. Li, R. J. Braun, K. L. Maki, W. D. Henshaw, P. E. King-Smith, Tear film dynamics with evaporation, wetting, and time-dependent flux boundary condition on an eye-shaped domain. *Physics of Fluids* **1994**, *26* (5), 052101.